COMPUTER METHODS IN MATERIALS SCIENCE

2025, vol. 25, no. 1, 5–14
https://doi.org/10.7494/cmms.2025.1.1014

Development of a constitutive material model of Mo-Mn-Fe-Co-Ni high entropy alloy through a structured two-phase inverse analysis

Aitor Orbea Larrañaga[1]*, Joseba Mendiguren Olaeta[1], Kamil Cichocki[2], Łukasz Madej[2]

[1] Mondragon Unibertsitatea, Loramendi 4, 20500 Mondragon, Spain.
[2] AGH University of Krakow, al. A. Mickiewicza 30, 30-019, Krakow, Poland.

Abstract

High entropy alloys, characterized by their near-equimolar compositions of five or more elements, exhibit unique properties including high strength, thermal stability, and corrosion resistance, making them ideal candidates for demanding applications. Unfortunately, experimental research on their behavior under processing and in-use conditions is expensive and time-consuming. Therefore, the use of computer-aided technology design is required. However, reliable constitutive material models for these alloys are rarely available in the literature. Thus, this research aims to develop a constitutive material model of a Mo-Mn-Fe-Co-Ni high entropy alloy through a structured two-phase inverse analysis. First, a preliminary inverse analysis was conducted to recalculate load-displacement data measured during uniaxial compression tests at varied temperatures and strain rates to the required flow stress data. This first phase helps mitigate the impact of testing artifacts – such as friction and localized heating – that can introduce inhomogeneities in the material and affects the hardening behavior. Then, a full inverse analysis was performed to precisely calibrate the constitutive model parameters, ensuring an accurate representation of the alloy's flow stress behavior under the tested conditions. This second phase optimizes the model to reflect the material's inherent properties rather than external test-induced effects, thus improving the robustness and reliability of the flow stress data across a range of loading scenarios. As a result, a reliable form of the constitutive model, along with the identified parameters, was obtained and can be used during computer-aided technology design.

Keywords: flow stress model, high entropy alloy, inverse analysis

1. Introduction

High entropy alloys represent an innovative class of materials distinguished by their near-equimolar compositions of five or more principal elements (Yeh et al., 2004). This distinctive multi-element structure imparts unique properties, including high mechanical strength, remarkable thermal stability, and superior resistance to corrosion and wear. These qualities make these alloys highly attractive for applications in sectors where materials face extreme conditions, such as aerospace, automotive, and energy industries. As high entropy alloys continue to receive interest for such demanding applications, the development of accurate material models is essential to simulate their behavior and enable predictive finite element simulations as a tool for computer-aided technology design.

* Corresponding author: aitor.orbea@alumni.mondragon.edu
ORCID ID's: 0009-0000-5005-6043 (A. O. Larrañaga), 0000-0002-2912-9030 (J. Mendiguren), 0000-0001-9183-8068 (K. Cichocki), 0000-0003-1032-6963 (Ł. Madej)

For finite element simulations to yield meaningful insights, robust constitutive models are required to represent the complex responses of high entropy alloys under various mechanical and thermal loading conditions. However, compositional complexity presents unique challenges for traditional material models, which often fall short of capturing the heterogeneities and non-linear responses characteristic of these alloys. Testing conditions such as friction, deformation-induced heating, and localized material responses can lead to inhomogeneities within the test samples, skewing the stress-strain data and limiting the accuracy of the resulting model. These factors underscore the need for advanced methods to minimize the test-induced influence of artifacts, thus ensuring reliable flow stress data.

Inverse analysis has emerged as an effective approach to address these limitations, offering a systematic method to calibrate constitutive models for various materials (Zhang et al., 2014). Unlike classical analytical methods, inverse analysis integrates experimental data with optimization algorithms to account for and mitigate testing inconsistencies and artifacts (Szeliga et al., 2006).

By interpreting test data through a finite element model, inverse analysis enables the identification of accurate material parameters that reflect the intrinsic behavior of high entropy alloys, independent of testing variables. This technique enhances model accuracy and improves the reliability of finite element simulations, supporting more effective integration of investigated alloys into real-world applications (Van Tonder et al., 2023).

This study aims to obtain reliable flow stress data and identify an optimal constitutive model for the Mo-Mn-Fe-Co-Ni alloy designed for subsequent metal forming operations (Cichocki et al., 2022). The initial phase focuses on refining raw test data to address artifacts and enhance data consistency, creating a stable foundation for model development. In the second phase, a comprehensive inverse analysis is performed to calibrate the model parameters, ensuring an accurate representation of the alloy's stress-strain behavior across various processing conditions. The resulting model is expected to provide a robust basis for future finite element simulations, addressing current limitations in high entropy alloy characterization and enabling more accurate predictions of material behavior under forming conditions and for in-use applications.

2. Experimental procedure

The experimental procedure involved uniaxial compression tests performed with an ASP machine (Fig. 1) on the Mo-Mn-Fe-Co-Ni high entropy alloy to obtain the necessary load-displacement data for model development. These tests were conducted at three different temperatures (900°C, 1,000°C, and 1,100°C) and three strain rates (0.1 s^{-1}, 1.0 s^{-1}, and 10.0 s^{-1}), covering a range of conditions representative of industrial applications.

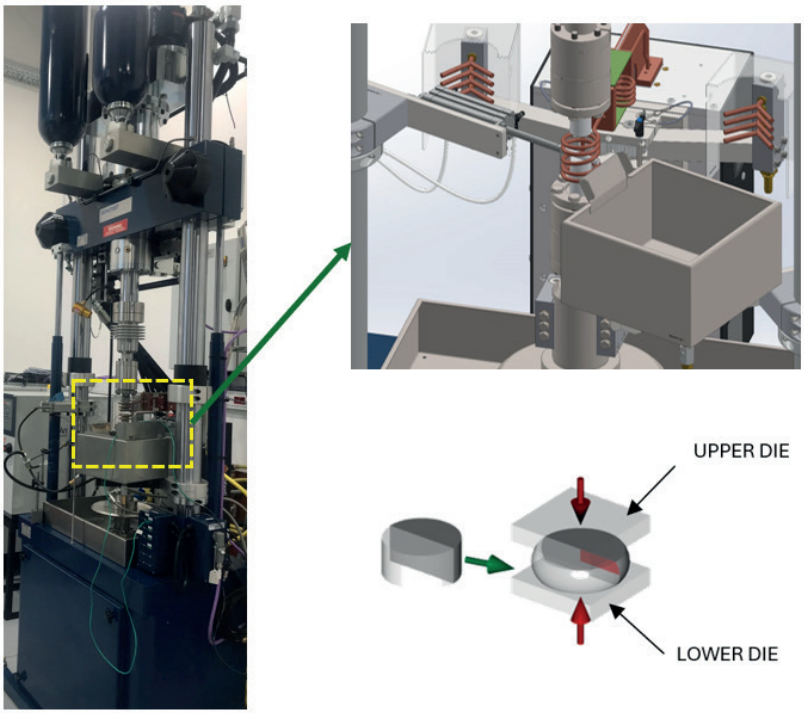

Fig. 1. ASP machine and representation of uniaxial compression tests

The ASP tests provided load-displacement curves for a combination of each temperature and strain rate. Figure 2 shows an example of the result obtained in the form of load-displacement data for 900°C and 0.1 1/s case. The experimental data were additionally subjected to smoothing operation to reduce the measurement noise.

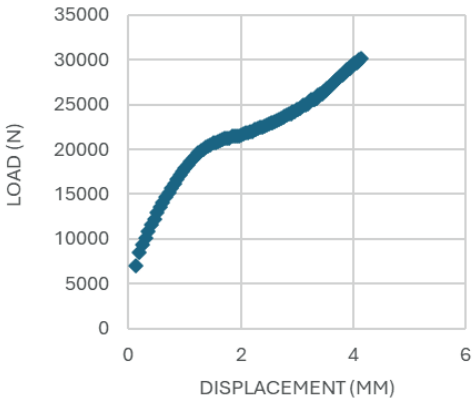

Fig. 2. Load-displacement curve at 900°C and 0.1 1/s test conditions

3. First phase inverse analysis

The preliminary inverse analysis was conducted to refine the load-displacement data obtained from uniaxial compression tests and convert it into reliable stress-strain curves for the subsequent material model parameter identification stage. This step aimed to mitigate the effects of testing artifacts, such as friction and localized deformation heating, which can lead to inaccuracies in flow stress data predictions and affect the reliability of finite element simulations (Lin et al., 2010).

The preliminary inverse analysis involved the following steps for all nine sets of load-displacement data recorded during UC (Fig. 3):

1. Acquiring the test's experimental results (load-displacement data) (uniaxial compression).
2. Develop a direct problem model based on the FE simulation that replicates the experimental uniaxial compression test.
3. Compare experimental load-displacement data with FE simulation ones to calculate the defined goal function, which measures the error of the simulated results with respect to the experimental curves.
4. Minimize the goal function ($\Phi(x)$) with the simplex optimization method, where key parameters – such as flow stress coefficient – were iteratively adjusted until the correlation between experimentally measured and numerically calculated values, reached an acceptable threshold (for details see: Kowalski et al., 2006).
5. Repeat steps 2 and 3 until the error between the experimental test and FE output is below the expected value.

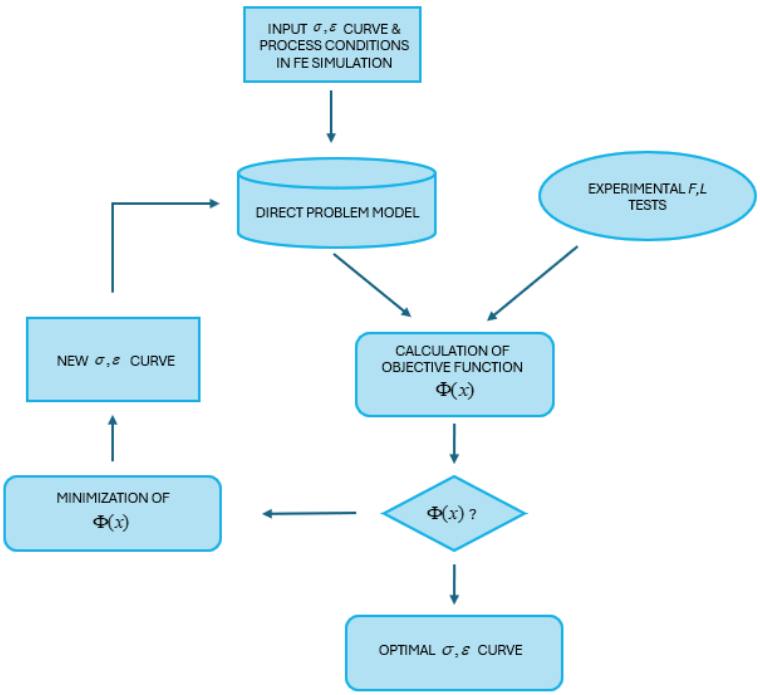

Fig. 3. Preliminary inverse analysis flow chart

The direct problem model was created using custom in-house FE software based on flow formulation principles (Gawad et al., 2005). The final correlation between the experimentally measured and numerically calculated load-displacement values, achieved through simplex optimization, is shown in Figure 4.

As presented, the difference is almost unnoticeable; thus, the reliability of the flow curves presented in Figure 5 is ensured.

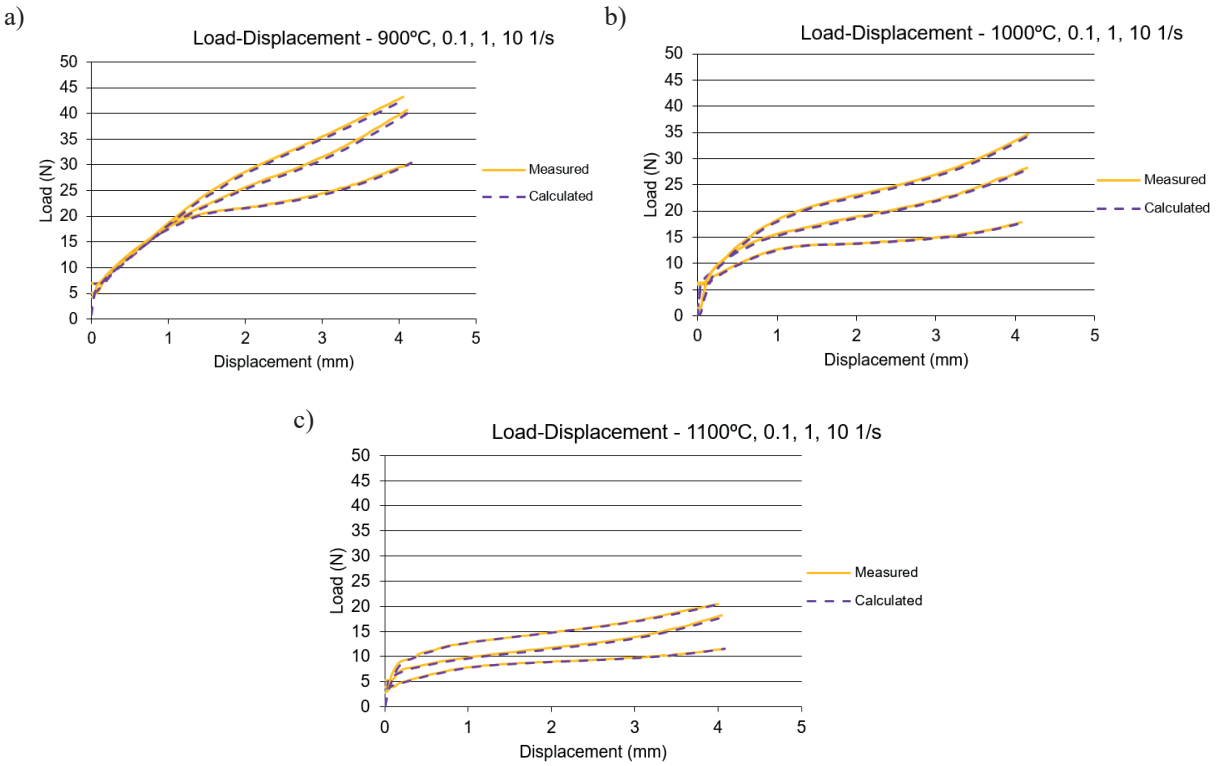

Fig. 4. Agreement between calculated and measured load-displacement data after the inverse analysis, 0.1 1/s, 1.0 1/s and 10.0 1/s strain rates at temperatures: a) 900°C; b) 1,000°C; c) 1,100°C

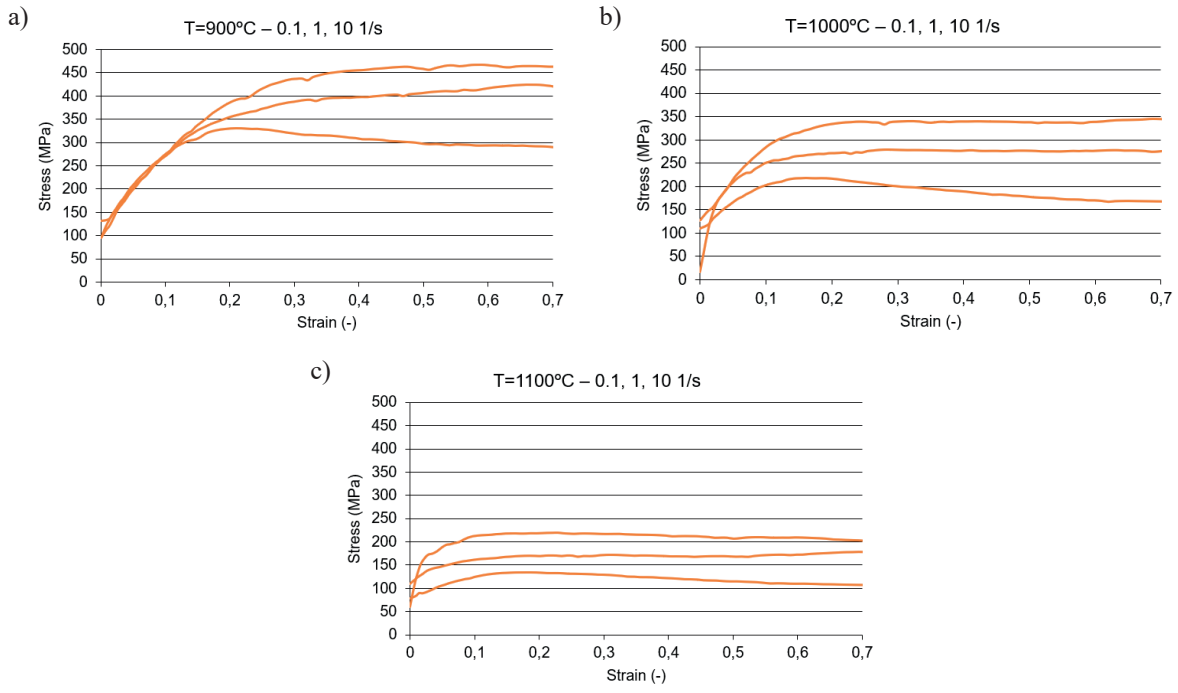

Fig. 5. Calculated stress-strain data after the inverse analysis, 0.1 1/s, 1.0 1/s and 10.0 1/s strain rates at temperatures: a) 900°C; b) 1,000°C; c) 1,100°C

4. Second phase inverse analysis

Various mathematical equations linking flow stress with strain, strain rate and temperature were investigated to develop a constitutive model for the Mo-Mn-Fe-Co-Ni high entropy alloy. The primary goal of the second phase of inverse analysis was to determine which model generates stress-strain curves that closely match the experimental data from the first phase of inverse analysis, thereby providing the most accurate representation of the alloy's mechanical behavior under the loading conditions.

The Hansel–Spittel model served as the base due to its flexibility in describing the effects of strain, strain rate, and temperature. Two modifications of this model were also explored, incorporating adjustments to the mathematical structure to assess their potential for the better replication of the experimental data. Additionally, the Johnson–Cook model was evaluated as a comparative benchmark for its simplicity and widespread application in metallic systems.

The procedure for the second-phase inverse analysis is illustrated in the flow chart (Fig. 6). The applied procedure involved the following steps:

1. Input an initial set of parameters into the chosen mathematical equation to generate stress-strain curves for all nine process conditions (combining strain rates and temperatures).
2. Compare the equation-predicted stress-strain curves with the experimental curves obtained from the first-phase inverse analysis.
3. Calculate the goal function ($\Phi(x)$), defined as the error between the equation-predicted and experimental curves.
4. Minimize $\Phi(x)$, iteratively adjusting the parameters of the equation.
5. Repeat steps 2 to 4 until the error between the predicted and experimental curves is below a predefined threshold.

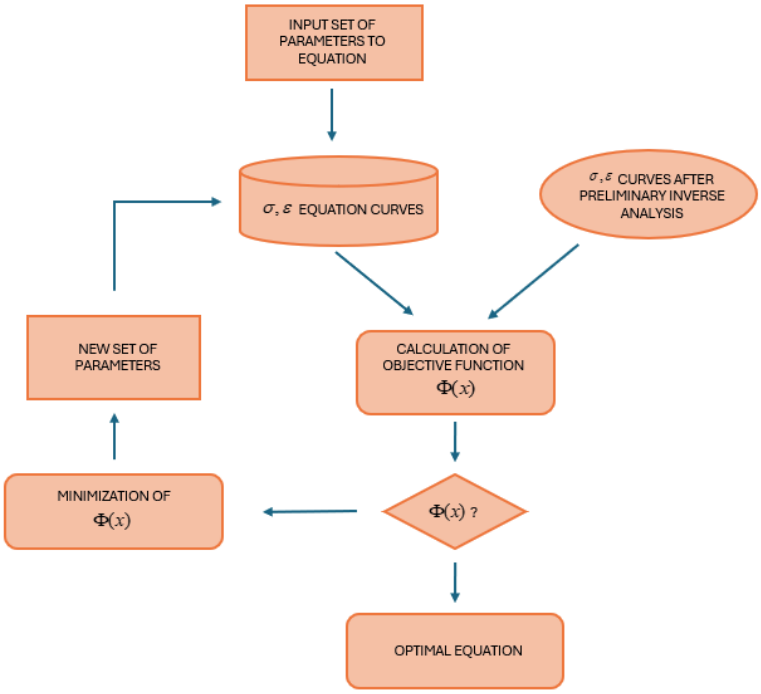

Fig. 6. Full inverse analysis flow chart

The identified model parameters are presented directly in the investigated Equations (1–7):

– the standard Hansel–Spittel (Chadha et al., 2018):

$$\sigma = 299{,}96 \cdot e^{-0{,}0025T} T^{0{,}173514} \varepsilon^{0{,}4176} e^{\frac{0{,}000628}{\varepsilon}} (1+\varepsilon)^{-0{,}00435167T} e^{1{,}81541\varepsilon} \dot{\varepsilon}^{-0{,}1299} \dot{\varepsilon}^{0{,}000218T} \quad (1)$$

where: σ – flow stress, ε – equivalent strain, T – temperature, $\dot{\varepsilon}$ – equivalent strain rate.

– the Johnson–Cook model:

$$\sigma = (-11631{,}3 + 15210 \cdot \varepsilon^{-0{,}0294123})(1 + 11{,}52 \cdot \ln(\dot{\varepsilon}^*))(1 - T^{*0{,}001562}) \quad (2)$$

where: σ – flow stress, ε – equivalent strain, T^* – homologous temperature, $\dot{\varepsilon}_0$ – quasi-static strain rate. T^* is expressed as $T^* = (T - T_{room})/(T_{melt} - T_{room})$, where T – temperature of the specimen and $\dot{\varepsilon}^* = \dot{\varepsilon}/\dot{\varepsilon}_0$.

– the modified Hansel–Spittel case 1 (Niu et al., 2021):

$$\sigma = \left\{ \exp(-a_7\varepsilon) a_1 \varepsilon^{a_2} \exp\left[\frac{a_4}{R(T+273)}\right] + (1-W) a_5 \exp\left[\frac{a_6}{R(T+273}\right] \right\} \dot{\varepsilon}^{a_3} \tag{3}$$

$$W = \exp(-a_7\varepsilon) \tag{4}$$

$$\sigma = \left\{ \exp(-0,79717 \cdot \varepsilon) \cdot 26,18 \varepsilon^{0,3454} \exp\left[\frac{32103,895}{R(T+273)}\right] + (1-W) \cdot 2,6187 \exp\left[\frac{-398242,961}{R(T+273)}\right] \right\} \dot{\varepsilon}^{0,08} \tag{5}$$

$$W = \exp(-0,79717 \cdot \varepsilon) \tag{6}$$

where: a_1–a_7 – coefficients, σ – flow stress, ε – equivalent strain, T – temperature, $\dot{\varepsilon}$ – equivalent strain rate and R – gas constant.

– the modified Hansel–Spittel case 2 (Wu et al., 2018):

$$\sin(0,005596 \cdot \sigma) = 3772,65 \cdot e^{-0,0064T} \varepsilon^{0,44089} \cdot \dot{\varepsilon}^{0,178452} e^{\frac{0,000521}{\varepsilon}} (1+\varepsilon)^{-0,029316T} e^{-1,47717\varepsilon} \tag{7}$$

where: σ – flow stress, ε – equivalent strain, T – temperature, $\dot{\varepsilon}$ – equivalent strain rate.

The corresponding stress-strain predictions and comparison with experimental data for each tested model are shown in Figures 7–10.

As presented in Figure 7, in the 1,000°C and 1,100°C graphs, the error of the standard Hansel–Spittel model at the beginning of hardening is unnoticeable, with deviations below 5 MPa. However, neither peak stress nor softening are successfully approximated, with peak stress deviations reaching up to approximately 30 MPa. The only reliable approximation is 1,100°C and 0.1 1/s, where deviations remain below 10 MPa throughout the curve.

In 900°C, flow stress predictions for the lowest and highest strain rates are not accurate. Hardening, peak stress, and softening in 0.1 1/s show significant errors, with peak stress underestimations around 35 MPa and softening deviations reaching 30 MPa. Although softening in 10.0 1/s is accurately captured, hardening is overestimated by approximately 25 MPa.

Figure 8 indicates that this model is not suitable for the investigated material. Comparing the error with the standard Hansel–Spittel model, the difference is staggering. In each of the nine curves, the error in hardening, peak stress, and softening is very large; not even the general shape of the graph is well represented.

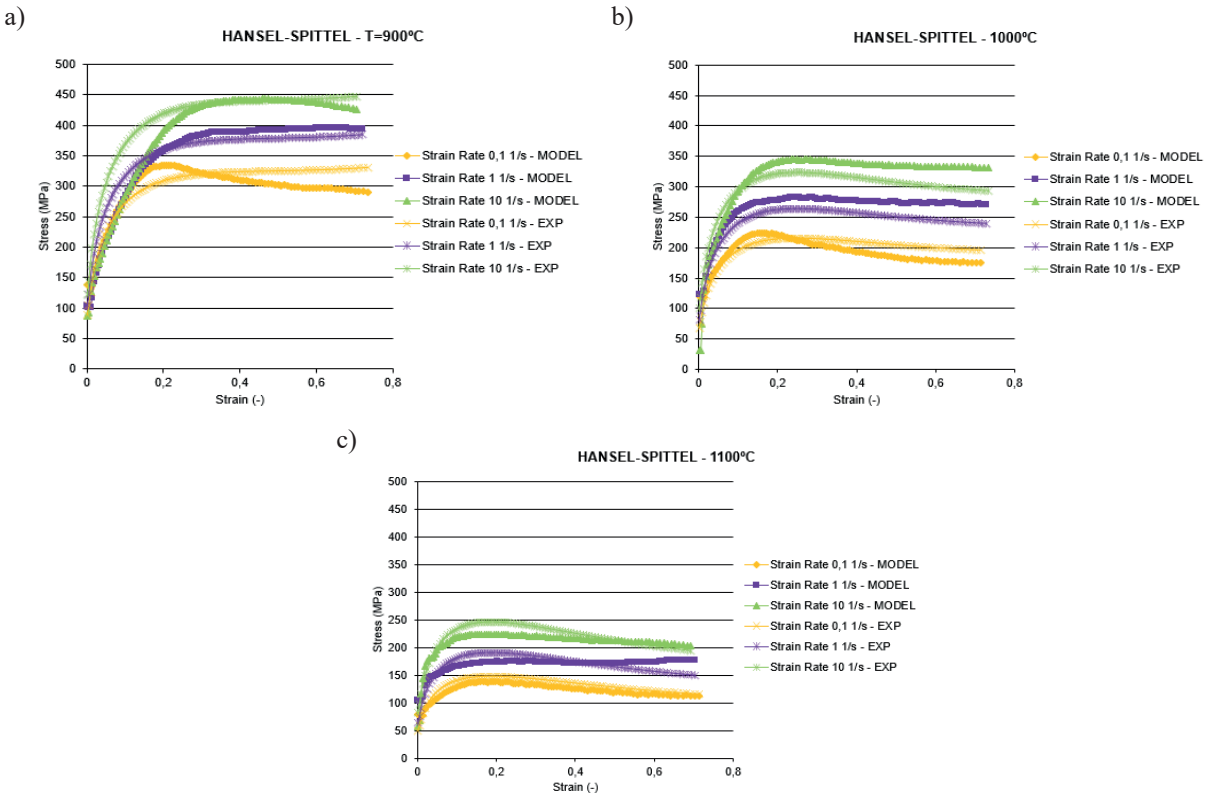

Fig. 7. Hansel–Spittel curves, for 0.1 1/s, 1.0 1/s and 10.0 1/s strain rates at temperatures: a) 900°C; b) 1,000°C; c) 1,100°C

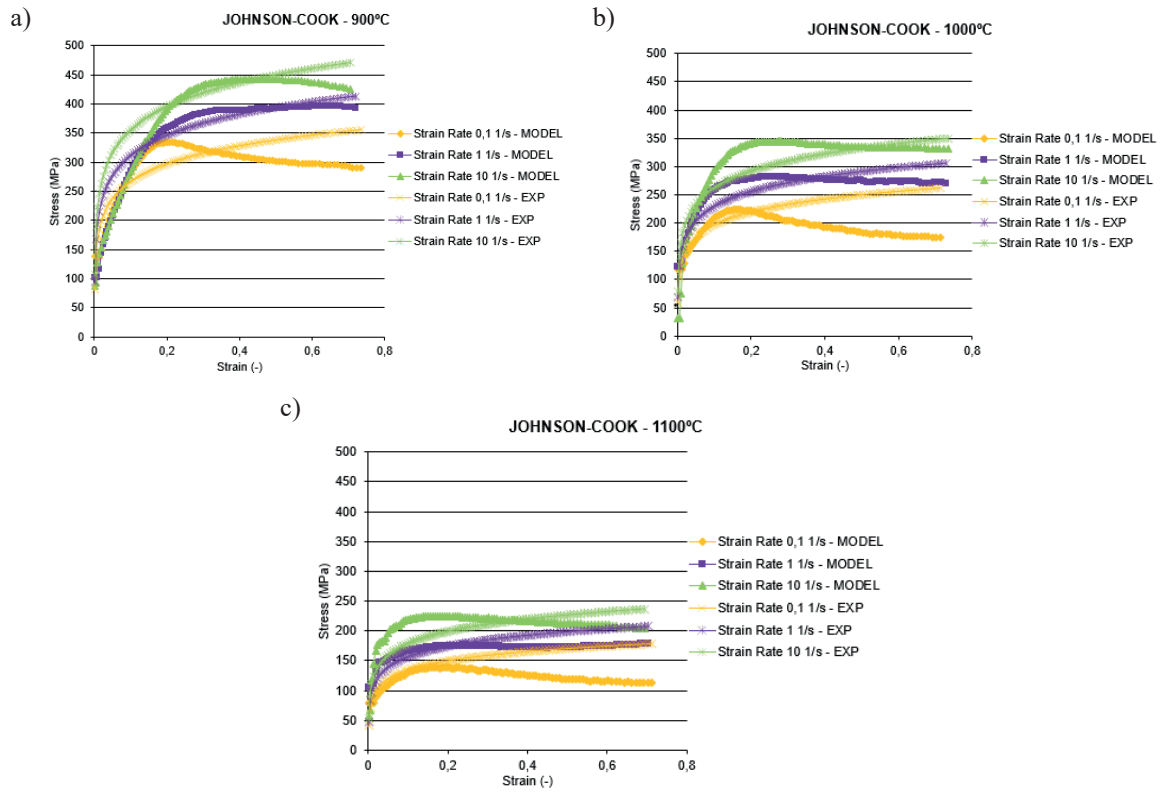

Fig. 8. Johnson–Cook curves, for 0.1 1/s, 1.0 1/s and 10.0 1/s strain rates at temperatures: a) 900°C; b) 1,000°C; c) 1,100°C

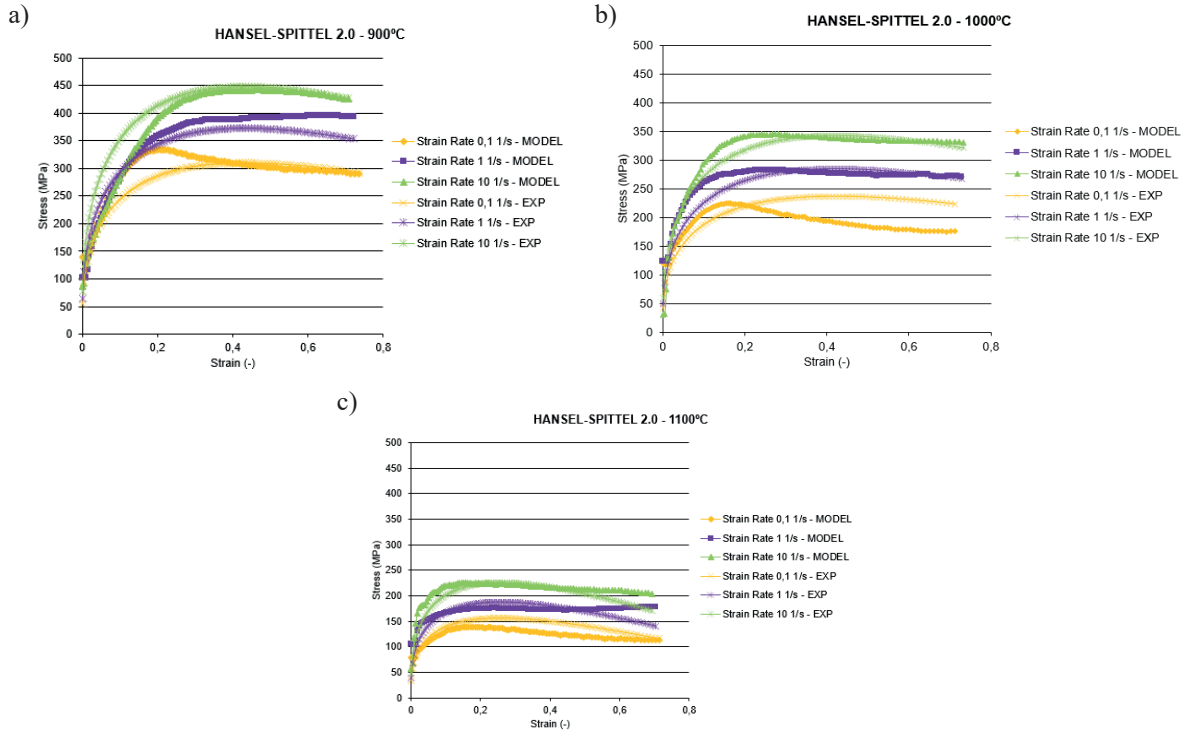

Fig. 9. Hansel–Spittel case 1 curves, for 0.1 1/s, 1.0 1/s and 10.0 1/s strain rates at temperatures: a) 900°C; b) 1,000°C; c) 1,100°C

As presented in Figure 9, for the modified Hansel–Spittel case 1, at 900°C, the curves at 0.1 1/s, 1.0 1/s, and 10.0 1/s adequately represent softening, but errors in hardening are noticeable, with stress deviations reaching up to 40 MPa at 10.0 1/s and 50 MPa at 1.0 1/s. The opposite situation occurs in the curve

at 1.0 1/s, where the precision in capturing hardening behavior is good, but deviations increase in the final strain stages, reaching up to 50 MPa. Regarding the graph at 1,000°C, at 10.0 1/s and 1.0 1/s, the approximation in softening is very good, with deviations remaining below 5 MPa, and the hardening part is partially captured; however, it shows slight deviations reaching up to approximately 20 MPa. Conversely, at 0.1 1/s, neither hardening nor softening are well approximated, and furthermore, the curve does not have the same general shape, resulting in peak stresses occurring at very different strains. At 1,100°C, each of the curves shows some level of deviation. At 10 and 11/s, softening is poorly represented, with deviations reaching up to approximately 30 MPa, and peak stresses do not coincide, occurring at slightly different strain values. Additionally, errors in the initial hardening range reach approximately 15 MPa. The curve at 0.1 1/s has a similar general shape, but from the middle of the hardening phase, deviations start to increase, reaching approximately 20 MPa.

Finally, predictions from the modified Hansel–Spittel case 2 from Figure 10 indicate that for the 900°C, in 0.1 1/s curve, the softening is perfectly represented (deviations remaining below 10 MPa at higher strains) while there are deviations of approximately 20 MPa in hardening and peak stress. For the other two strain rates, hardening is poorly approximated. At 10.0 1/s, there is an overestimation of up to 150 MPa, and at 1 1/s, the overestimation reaches nearly 100 MPa. In both cases, the peak stress occurs at a much lower strain, approximately 0.2 strain, compared to the experimental value. Additionally, the softening phase does not adequately capture the stress decrease, resulting in deviations reaching up to 40 MPa at the final stages. At 1,000°C and at 10.0 1/s, the peak stress is very precise but hardening and softening are not well approximated. At 0.1 1/s, the hardening part is well recreated, but peak stress occurs earlier than in the experiment, and the softening part is not accurately captured. Conversely, at 1.0 1/s, the curve is almost the same until it deviates starting from a strain of 0.5. Finally, the curves at 1,100°C are the most precise. The three curves are almost identical, except for a difference of approximately 10 MPa in the hardening at 0.1 1/s and 1.0 1/s, a slight deviation starting from a strain rate of 0.6, reaching up to 25 MPa at the highest strains for 1.0 1/s, and a difference of around 10 MPa in softening at 10.0 1/s.

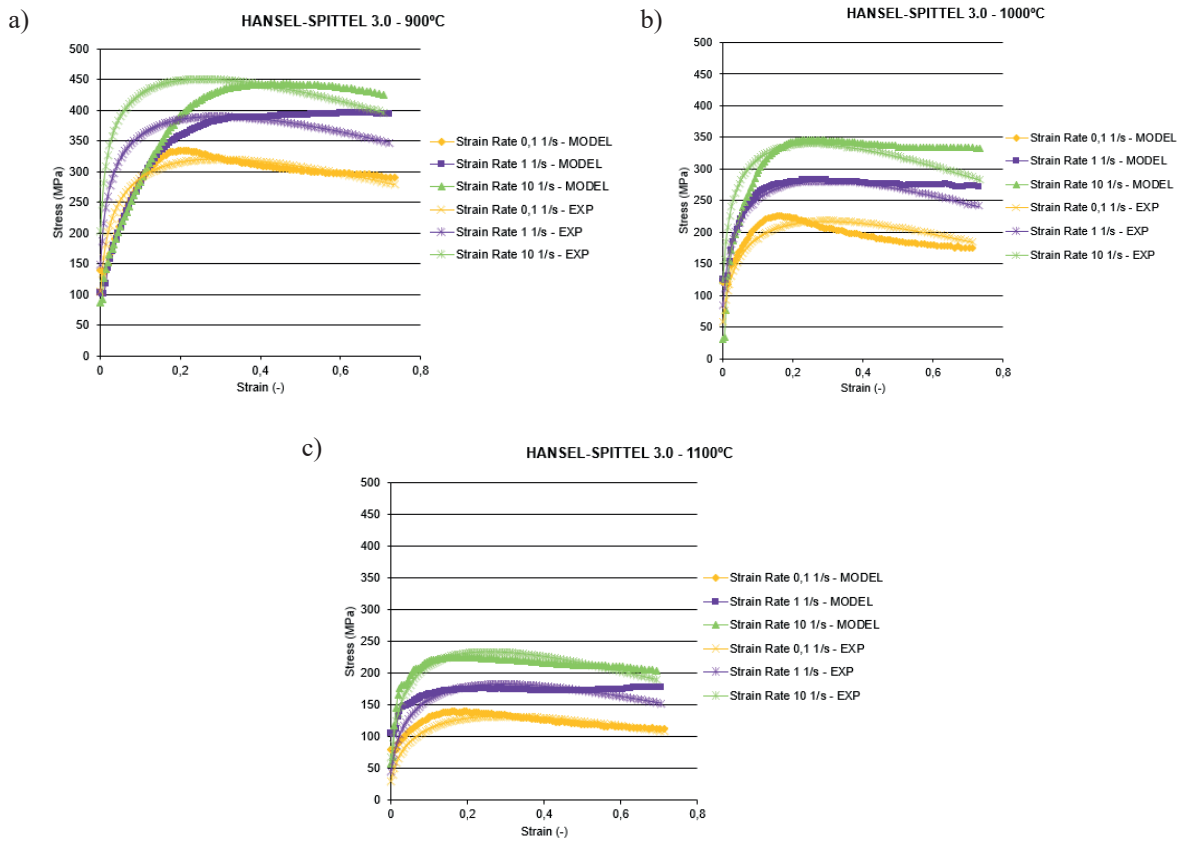

Fig. 10. Hansel–Spittel case 2 curves, for 0.1 1/s, 1.0 1/s and 10.0 1/s strain rates at temperatures: a) 900°C; b) 1,000°C; c) 1,100°C

Therefore, based on the presented investigations, it can be summarized that the last model in the form of modified Hansel–Spittel case 2 demonstrated the best alignment with the experimental data among the evaluated options. As a result, this model should be used in further finite element simulations of processing or exploitation conditions as the most reliable. While some discrepancies remain between the model predictions and experimental results, they are within acceptable margins for practical applications. These deviations are expected due to the inherent challenge of fitting a single constitutive equation to a wide range of strain rates and temperatures. Despite this, similar levels of inaccuracy – typically within a 7–10% range of absolute error – are common in constitutive modeling of complex alloys (Laplanche et al., 2016; Miracle & Senkov, 2017; Zhang et al., 2014), and do not significantly impact the reliability of numerical simulations in industrial forming processes.

5. Conclusions

Based on the presented investigation, it can be concluded that using the two-phase inverse analysis allows for the efficient development of a reliable constitutive model for the investigated Mo-Mn-Fe-Co-Ni high entropy alloy. These results underscore the robustness and reliability of the modified Hansel–Spittel case 2 model, which consistently replicated experimental observations across varying conditions. At 1,100°C, the model closely matched experimental data for all strain rates, exhibiting minimal deviations in hardening and softening regions. At 1,000°C, it accurately predicted the peak stresses while showing slight discrepancies in the softening phase at lower strain rates. At 900°C, the model effectively captured the softening behavior at a strain rate of 0.1 s^{-1}, although minor errors were observed in the hardening region.

Therefore, the modifications introduced to the original Hansel–Spittel framework significantly improved its predictive accuracy, particularly in capturing the transitions between hardening and softening phases.

Such a constitutive model can then be successfully used for the finite element simulations of this high entropy alloy response under processing or exploitation conditions, providing a reliable foundation for understanding and optimizing its deformation behavior. In addition, considering the compositional variability inherent to high entropy alloys, it is relevant to discuss the applicability of this approach to other alloy systems. The inverse analysis methodology presented in this study can be extended to other high entropy alloys within the same compositional system, provided that the dominant deformation mechanisms and phase stability remain unchanged. Prior research has demonstrated that minor compositional variations can preserve key mechanical properties when the solid solution strengthening and dislocation-based hardening mechanisms are consistent (Miracle & Senkov, 2017; Zhang et al., 2014). However, substantial compositional shifts, particularly those altering the stacking fault energy or phase stability, have been shown to significantly modify strain-hardening behavior and flow stress evolution (Gao et al., 2016). In such cases, a re-evaluation of material parameters is necessary to ensure the accurate characterization and predictive capability of the model.

References

Chadha, K., Shahriari, D., & Jahazi, M. (2018). An approach to develop Hansel–Spittel constitutive equation during ingot breakdown operation of low alloy steels. In M. Muruganant, A. Chirazi, B. Raj (Eds.), *Frontiers in Materials Processing, Applications, Research and Technology. Select Proceedings of FiMPART 2015* (pp. 239–246). Springer Singapore. https://doi.org/10.1007/978-981-10-4819-7_20

Cichocki, K., Bała, P., Kozieł, T., Cios, G., Schell, N., & Muszka, K. (2022). Effect of Mo on phase stability and properties in FeMnNiCo high-entropy alloys. *Metallurgical and Materials Transactions A: Physical Metallurgy and Materials Science*, *53*(5), 1749–1760. https://doi.org/10.1007/s11661-022-06629-x

Gao, M. C., Yeh, J.-W., Liaw, P. K., & Zhang, Y. (2016). *High-entropy alloys: Fundamentals and applications*. Springer Cham. https://doi.org/10.1007/978-3-319-27013-5

Gawad, J., Kuziak, R., Madej, L., Szeliga, D., & Pietrzyk, M. (2005). Identification of rheological parameters on the basis of various types of compression and tension tests. *Steel Research International*, *76*(2–3), 131–137. https://doi.org/10.1002/srin.200505984

Kowalski, B., Sellars, C. M., & Pietrzyk, M. (2006). Identification of rheological parameters on the basis of plane strain compression tests on specimens of various initial dimensions. *Computational Materials Science*, *35*(2), 92–97. https://doi.org/10.1016/j.commatsci.2005.02.024

Laplanche, G., Kostka, A., Horst, O. M., Eggeler, G., & George, E. P. (2016). Microstructure evolution and critical stress for twinning in the CrMnFeCoNi high-entropy alloy. *Acta Materialia*, *118*, 152–163. https://doi.org/10.1016/j.actamat.2016.07.038

Lin, Y.-K., Hsu, K.-M., & Lee, P.-K. (2010). The application of flow stress model to sheet metal forming simulation. *China Steel Technical Report*, *23*, 49–55.

Miracle, D. B., & Senkov, O. N. (2017). A critical review of high entropy alloys and related concepts. *Acta Materialia*, *122*, 448–511. https://doi.org/10.1016/j.actamat.2016.08.081

Niu, L., Zhang, Q., Wang, B., Han, B., Li, H., & Mei, T. (2021). A modified Hansel-Spittel constitutive equation of Ti-6Al-4V during cogging process. *Journal of Alloys and Compounds*, *894*, 162387. https://doi.org/10.1016/j.jallcom.2021.162387

Szeliga, D., Gawad, J., & Pietrzyk, M. (2006). Inverse analysis for identification of rheological and friction models in metal forming. *Computer Methods in Applied Mechanics and Engineering*, *195*(48–49), 6778–6798. https://doi.org/10.1016/j.cma.2005.03.015

Van Tonder, J. D., Venter, M. P., & Venter, G. (2023). A new method for improving inverse finite element method material characterization for the Mooney–Rivlin material model through constrained optimization. *Mathematical and Computational Applications*, *28*(4), 78. https://doi.org/10.3390/mca28040078

Yeh, J.-W., Chen, S.-K., Lin, S.-J., Gan, J.-Y., Chin, T.-S., Shun, T.-T., Tsau, C.-H., & Chang, S.-Y. (2004). Nanostructured high-entropy alloys with multiple principal elements: Novel alloy design concepts and outcomes. *Advanced Engineering Materials*, *6*(5), 299–303. https://doi.org/10.1002/adem.200300567

Zhang, Y., Zuo, T. T., Tang, Z., Gao, M. C., Dahmen, K. A., Liaw, P. K., & Lu, Z. P. (2014). Microstructures and properties of high-entropy alloys. *Progress in Materials Science*, *61*, 1–93. https://doi.org/10.1016/j.pmatsci.2013.10.001